

---

## Full-length paper

# Four-dimensional dielectric property image obtained from electron spectroscopic imaging series

Shen-Chuan Lo<sup>1,\*</sup>, Ji-Jung Kai<sup>1</sup>, Fu-Rong Chen<sup>1</sup>, Li Chang<sup>2</sup>, Li-Chien Chen<sup>1</sup>, Cheng-Cheng Chiang<sup>1</sup>, Peijun Ding<sup>3</sup>, Barry Chin<sup>3</sup>, Hong Zhang<sup>3</sup> and Fusen Chen<sup>3</sup>

<sup>1</sup>Department of Engineering and System Science, National Tsing-Hua University HsinChu, 300 Taiwan,

<sup>2</sup>Department of Materials Science and Engineering, National Chiao-Tung University HsinChu, 300 Taiwan and

<sup>3</sup>Applied Materials, Santa Clara, CA 95054, USA

\*To whom correspondence should be addressed. E-mail: d877110@oz.nthu.edu.tw

---

**Abstract** We have demonstrated a new quantitative method to characterize two-dimensional distributions of energy-dependent dielectric function of materials from low loss electron spectroscopic image (ESI) series. Two problems associated with extracted image-spectrum from the low-loss image series, under-sampling and loss of energy resolution, were overcome by using fast Fourier transformation (FFT) interpolation and maximum entropy deconvolution method. In this study, Black Diamond<sup>TM</sup>/Si<sub>3</sub>N<sub>4</sub>/SiO<sub>2</sub>/Si-substrate dielectric layer designed for copper metallization was used as the sample. We show that the reconstructed (FFT interpolated and maximum entropy deconvoluted) image-spectrum obtained from ESI series images can be quantified with the same accuracy as conventional electron energy-loss spectroscopy spectra. Since the analysis of the dielectric function is sensitive to the local thickness of the specimen using Kramers–Kronig analysis, we also developed a new method to quantitatively determine the dielectric constant for low-*k* materials. We have determined the thickness of the Black Diamond using the extrapolated thickness method from the materials of known dielectric constants. Using Kramers–Kronig formula, the dielectric function map can be deduced from two-dimensional reconstructed single scattering spectra with providing the information of thickness. We proposed a four-dimensional data presentation for revealing the uniformity of the energy dependent property. The accuracy of our methods depends on the thickness determination and on the quality of the reconstructed spectra from the image series.

---

**Keywords** dielectric property image, electron spectroscopic image series, FFT interpolation, maximum entropy deconvolution, image-spectrum, Kramers–Kronig analysis

---

**Received** 15 December 2000, accepted 3 October 2001

---

## Introduction

Energy-filtered transmission electron microscopy (EFTEM) has become a very useful tool in characterizing material properties, because it allows the study of local chemical and electronic properties of a specimen at nanometre level spatial resolution [1–4]. Conventional EFTEM techniques utilize only two- or three-window methods to extract a two-dimensional elemental map [5,6] from inner-shell ionization edges occurring in electron energy-loss spectroscopy (EELS) spectrum.

The elemental map produced by the two- or three-window technique provides a rapid and efficient method for qualitative characterization. However, there is less study received for quantitative analysis with elemental maps. Basically, compositional quantitative analysis is commonly carried out by EELS spectrum. Two spectroscopic imaging methods have been established to obtain both the spatial and the spectral information,  $I(x, y, \Delta E)$ , which can be quantitatively evaluated. One technique, known as the spectrum-image method, is

based on scanning the electron beam across the sample to acquire the EELS spectrum with two-dimensional information [7–9]. Conversely, the other method retrieves the spectra in a specific position from a series of energy loss images, and is known as the image-spectrum method [10–18]. The spectrum-image method can be achieved with better energy resolution, but requires a long acquisition time. Compared to the spectrum-image method, the advantage of the image-spectrum method is the capability of simultaneously recording abundant information in a series of maps. Nevertheless, besides plural scattering, there are still two main problems, under-sampling and loss of energy resolution, existing in the spectrum retrieved from the image-spectrum method. The problem of under-sampling is due to moving the energy slit in a discrete energy space, and loss of the energy resolution is due to finite width of energy slit in imaging filter.

Recently, the image-spectrum method has been proposed to evaluate compositional [12–18] and thickness distribution [12–15] quantitatively, with tens of images recorded across core loss edges and the low-loss region, respectively. Basically, the spectra extracted from a series of ESI images are broadened by both the width of the energy slit and the under-sampling, as the images were obtained with an energy slit of finite width, and were discretely sampled in the energy space. The energy resolution of the extracted spectrum from a series of ESI is reduced due to the integrated intensity within the energy slit used. The extracted spectrum is identical to the convolution of a perfect spectrum with a point spread function (PSF), which is a flat hat function with a width equivalent to that of the energy slit. A perfect spectrum can be recovered from a maximum entropy deconvolution [19] by using a PSF and a spectrum extracted from a series of ESI images. Maximum entropy and Fourier-log deconvolutions [1,2] are considered for different purposes. Maximum entropy deconvolution can remove noise and recover weak signal information due to the finite width of the energy slit, while the Fourier-log method is generally employed to remove the plural scattering effect [2]. Data must be well constructed to reconstruct reliably the spectrum since a maximum entropy deconvolution process requires sufficient sampling points to approach a smooth, continuous spectrum. Data interpolation is required not only to yield high accuracy in deconvolution and thus remove the effect of the finite width of the energy slit, but also to reduce the data acquisition and the amount of data storage. Normally, a linear, spline or polynomial function was employed for data interpolation. In previous work [12–18], linear interpolation was used to supplement the data in the energy space. The under-sampling may not be problematic when analyses are based only on integrating the area under the spectrum, and may not be sensitive to the methods of interpolation. However, under-sampling may be crucial for conducting dielectric function and energy band gap analyses in the low-loss region, and determining the fine structure in the core-loss region where energy resolution may significantly influence the data analysis. The fine structure in the core-loss

region of EELS spectrum may have no simple relationship with the energy loss. Therefore, assuming a polynomial function to interpret data may lose physical meaning when the local fine structure in EELS spectrum is extracted. In this study, a fast Fourier transformation (FFT) interpolation [20] is used to solve the under-sampling in the image-spectrum. The merit of FFT interpolation over linear, polynomial or cubic spline methods, is that no relationship is assumed between the interpolated data and the original data points. FFT interpolation may be a good choice for universal interpolation in different ionization edges, since no mathematical model is employed. Moreover, in this paper, a constrained-maximum entropy method [21] originally designed to extend the spatial resolution for high-resolution image is now used to improve the energy resolution of the image-spectrum. The dielectric function, therefore, can be deduced from low-loss region of image-spectrum, with sufficient sampling and energy resolution with the regular Kramers–Kronig analyses [2]. Finally, we have proposed a four-dimensional data presentation to reveal the special two-dimensional distribution of the energy dependent dielectric function [ $\epsilon_1 + i\epsilon_2, x, y, \Delta E$ ], which is called the property image.

Because of the rapid development of low-dielectric constant (low- $k$ ) materials in copper metallization for semiconductor device [22], the determination of dielectric constant in low- $k$  materials becomes very urgent. The dielectric constant can be determined from electrical measurements on metal-oxide-semiconductor (MOS) capacitors [23]. However, in patterning specimen, the conventional capacitance measurement is not feasible to determine the dielectric constant of low- $k$  material.

In this paper, Black Diamond™ (BD) is used to test the accuracy of our analysis methods. Black Diamond is a silicon oxide-based low- $k$  material, doped with a few percent of carbon and is designed by Applied Materials, USA, for the Cu metallization process. The mass density of BD ( $1.4 \text{ g cm}^{-3}$ ) indicates an estimate of porosity of 36% volume fraction of pores, with  $\text{SiO}_2$  ( $2.2 \text{ g cm}^{-3}$ ) as a reference. The dielectric constant of BD has been determined using capacitance measurement for reference [24].

## Experimental

This study was performed with a JEOL 2010F transmission electron microscope operated at 200 kV and equipped with a Schottky type of field emission gun (FEG) and a Gatan imaging filter (GIF). Electron spectroscopic image series were recorded on a Gatan 1024 × 1024 slow scan CCD-camera. The sample with structure of BD /  $\text{Si}_3\text{N}_4$  /  $\text{SiO}_2$  / Si-substrate was investigated. Black Diamond is a novel low- $k$  dielectric material, designed for the Cu metallization process by Applied Materials Company [24]. The composition of BD is unknown. A wedge-shaped TEM sample was prepared by special tripod polishing method [25]. An image series consisting of seventy-one ESI images was recorded from –10 to 60 eV loss with steps of 1 eV. The width of the energy-selecting slit was also set to

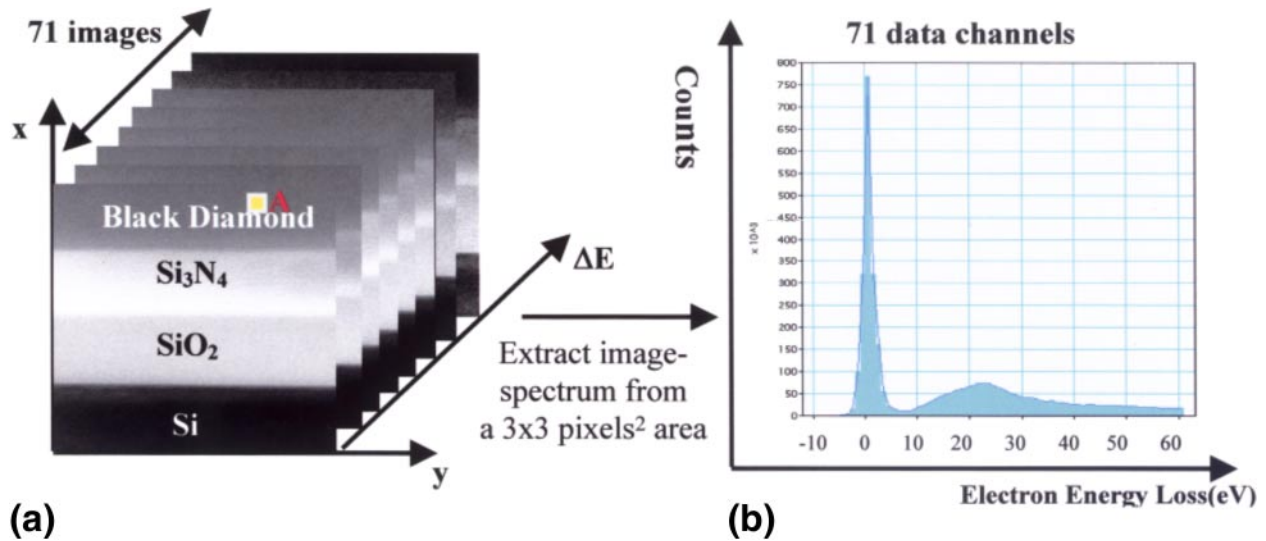


**Fig. 1** (a) Low-loss electron spectroscopic image series of BD/Si<sub>3</sub>N<sub>4</sub>/SiO<sub>2</sub>/Si from -10 to 60 eV. (b) A spectrum extracted from the electron spectroscopic image series with sampling size of  $3 \times 3$  pixels<sup>2</sup> in BD region.

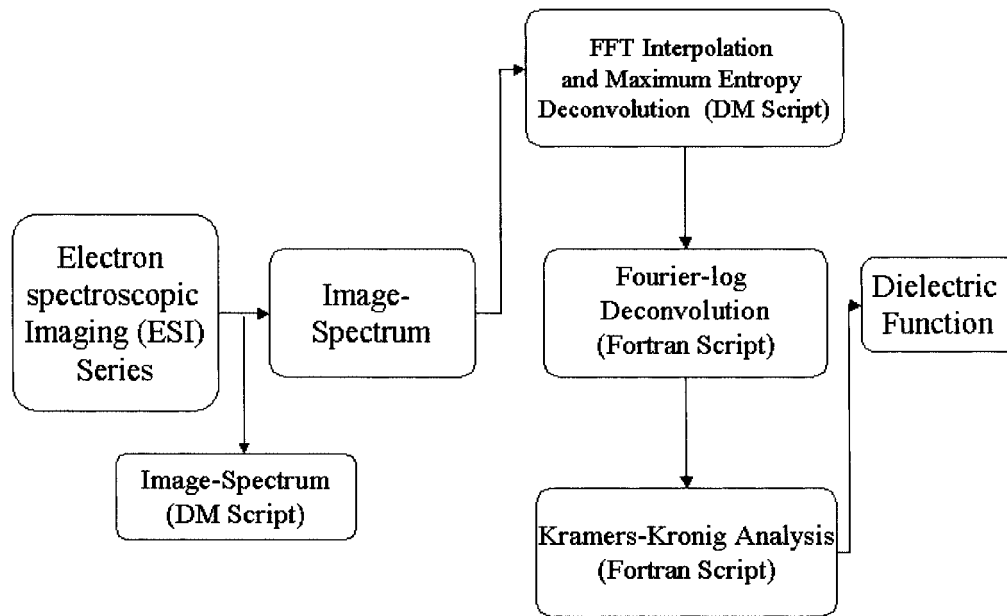


**Fig. 2** Flow chart of analytical method and algorithm.

be 1 eV. The exposure time of each image is 3 s. The collection semi-angle  $\beta$  is 10 mrad. The experimental image series is shown in Fig. 1a. All the images are aligned with the cross-correlation technique. The theoretical spatial resolution of an ESI image was estimated by the method of Krivanek *et al.* [26]. In their study, three factors (delocalization, chromatic aberration, and aperture diffraction limit) are considered to limit the theoretical spatial resolution in ESI image. In the FEG TEM presented here, the energy spread of the electron beam was optimized to about 1 eV for regular application. In this work, the theoretical spatial resolution of ESI images was evaluated at approximately 15.2 and 1.9 nm for a plasmon

energy loss of 5 and 50 eV, respectively.

As shown in Fig. 1a, each pixel within the image series can be treated as an individual EELS spectrum. The pixel resolution in the image is 0.94 nm per pixel. The image-spectra were extracted using the script language of Digital Micrograph software by integrating over  $3 \times 3$  pixels equivalent to an area of  $2.8 \times 2.8$  nm in the image. Figure 1b shows an extracted spectrum in BD from the image series. The dispersion (sampling energy step) of this extracted spectrum is 1 eV. The energy resolution in the extracted spectrum is lost due to the finite width of energy slit. As shown in Fig. 1b, the full-width at half-maximum (FWHM) of the zero-loss peak is roughly 1.6 eV.

The extracted spectra from the electron spectroscopic series images were reconstructed by FFT interpolation and deconvoluted by both maximum entropy and Fourier-log methods before quantitative analyses of dielectric function using Kramers–Kronig transformation. A flow chart of analytical procedures is demonstrated in Fig. 2. The details of the methodology and the algorithm are sequentially described in the next section. All the analysis programs are written in the script language of the Digital Micrograph software [27].

## Methodology and algorithm

### FFT interpolation

Interpolation by the FFT has become a practical proposition in many areas, such as image resampling, and digital signal processing (DSP) microcircuits [28]. The algorithm given here is basically modified from that suggested by Schafer and Rabiner [29]. Suppose that an extracted spectrum is denoted as  $S(\Delta E_i)$  which has  $N$  pixels.  $N$  is actually the number of electron spectroscopic images. The index  $i$  is from 0 to  $N - 1$ . Fourier transform of this spectrum is given as  $U(k)$ .

$$U(k) = \frac{1}{N} \sum_{i=0}^{N-1} S(\Delta E_i) \exp\left(\frac{-j2\pi ik}{N}\right),$$

where,  $k = -\frac{N}{2}, -\frac{N}{2} + 1, \dots, 0, \dots, \left(\frac{N}{2}\right) - 1$  (1)

Let us create a new interpolated sequence  $V(k)$ , having  $L = M \times N$  terms, where  $M$  is an integer that we call resampling multiplier. A folding frequency or Nyquist limit  $N_{\text{ny}}$  is the nearest rounding integer of  $(N + 1) / 2$ . The interpolation process basically involves folding the coefficients of  $U(k)$  to both end of new sequence  $V(k)$  and the zeros are added to the centre of  $V(k)$ . The  $V(k)$  is given as

$$V(k) = \begin{cases} U(k) & k = -(L/2), -(L/2)+1, \dots, -(L/2)+N_{\text{ny}}-1 \\ 0.5U(k) & k = -(L/2)+N_{\text{ny}} \quad (N \text{ even}) \\ U(k) & k = -(L/2)+N_{\text{ny}} \quad (N \text{ odd}) \\ 0 & k = -(L/2)+N_{\text{ny}}+1, \dots, (L/2)+N_{\text{ny}}+1-N \\ U(k) & k = (L/2)+N_{\text{ny}}+1-N, \dots, (L/2)-1 \end{cases} \quad (2)$$

Note that, if  $N$  is even, all terms are carried over to the new sequence with equal weighting except the term at the folding frequency  $k = -(L/2) + N_{\text{ny}}$ , which must be given a relative weighting of one half. If  $N$  is odd, all terms have equal weighting. If the spectrum is a real function, therefore, the  $U(k)$  in the last frequency domain is conjugated related to that in the first frequency domain. The new interpolated spectrum  $S'(\Delta E_i)$  with  $L$  pixels can be obtained by an inverse Fourier transform of  $V(k)$ . The originally extracted spectrum, presented in Fig. 1b, is interpolated to 0.125 eV dispersion by FFT interpolation. Figures 3a and 3b display two magnified spectra, to demonstrate the differences among the FFT, spline and linear interpolations in the energy region of zero loss and plasmon loss, respectively. The data from different interpolated methods are displayed separately to show clearly the differences among the

data from each method of interpolation. The black squares indicate the original data of the extracted spectrum, and the circles, triangles and crosses represent FFT, spline and linear interpolated data, respectively.

Linear interpolation produces a relatively rugged spectrum, while the FFT and spline methods give a smooth curve. The artefacts usually occur in the maximum entropy deconvolution process in a rugged spectrum, since such a deconvolution tends to enhance the weak peak signal. FFT, spline or polynomial interpolations might not show great differences in further maximum entropy deconvolution and might not be critical in determining the dielectric function which was determined from Kramers–Kronig method by using the area under the curve of plasmon loss. However, in the core-loss region, the sharp ionization edge is not simply, mathematically related to the fine structure in the EELS spectrum (by polynomial, cubic, or any other relationship). Different ionization edges are associated with different relationships. Accordingly, FFT interpolation could be a good choice for universally interpolating for different ionization edges, since such an interpolation involves no mathematical model. The artefact from FFT interpolation may occur when the spectrum contains a huge intensity difference. As shown in Fig. 3c, if the zero-loss peak and plasmon-loss peak are processed together, a small modulation may be induced in the lower intensity part, although this modulation is much smaller than the zero-loss peak. This small modulation can be removed either by separately processing the plasmon and zero-loss peak, or by a wavelet transformation.

### Maximum entropy deconvolution method

Overwijk and Reefman have used the maximum entropy method to remove the instrumental response function of the zero-loss peak [19]. In this paper, we adopt a constrained maximum entropy method (MEM) [21,30], which was designed to extend spatial resolution of high resolution images in a NiSi<sub>2</sub>/Si interface, to improve the energy resolution suffered from the finite width of energy slit. Our method is slightly different from that of Overwijk and Reefman in the constraint terms coupling with the entropy. In our study, maximum entropy method is used to deconvolute the finite energy slit effect from a FFT interpolated spectrum. Deconvolution is carried out by minimization of a Lagrangian function  $L$ , providing a known point spread function  $PSF(E_i)$  which is a flat hat function with a width equivalent to that of the energy slit.

$$L = -\sum_i S(E_i) \ln\left(\frac{S(E_i)}{D(E_i)}\right) - \lambda_0 \sum_i (S(E_i) - f) - \lambda_1 \sum_i [S(E_i) * PSF(E_i) - S^{\text{exp}}] \quad (3)$$

$S(E_i)$  is an optimum spectrum which we would like to find and  $E_i$  is a vector in the energy space. The  $i$  is an index of  $i$ th pixel in the spectrum. The summation is carried out on all pixels and  $S^{\text{exp}}$  is a spectrum after the FFT interpolation. The first

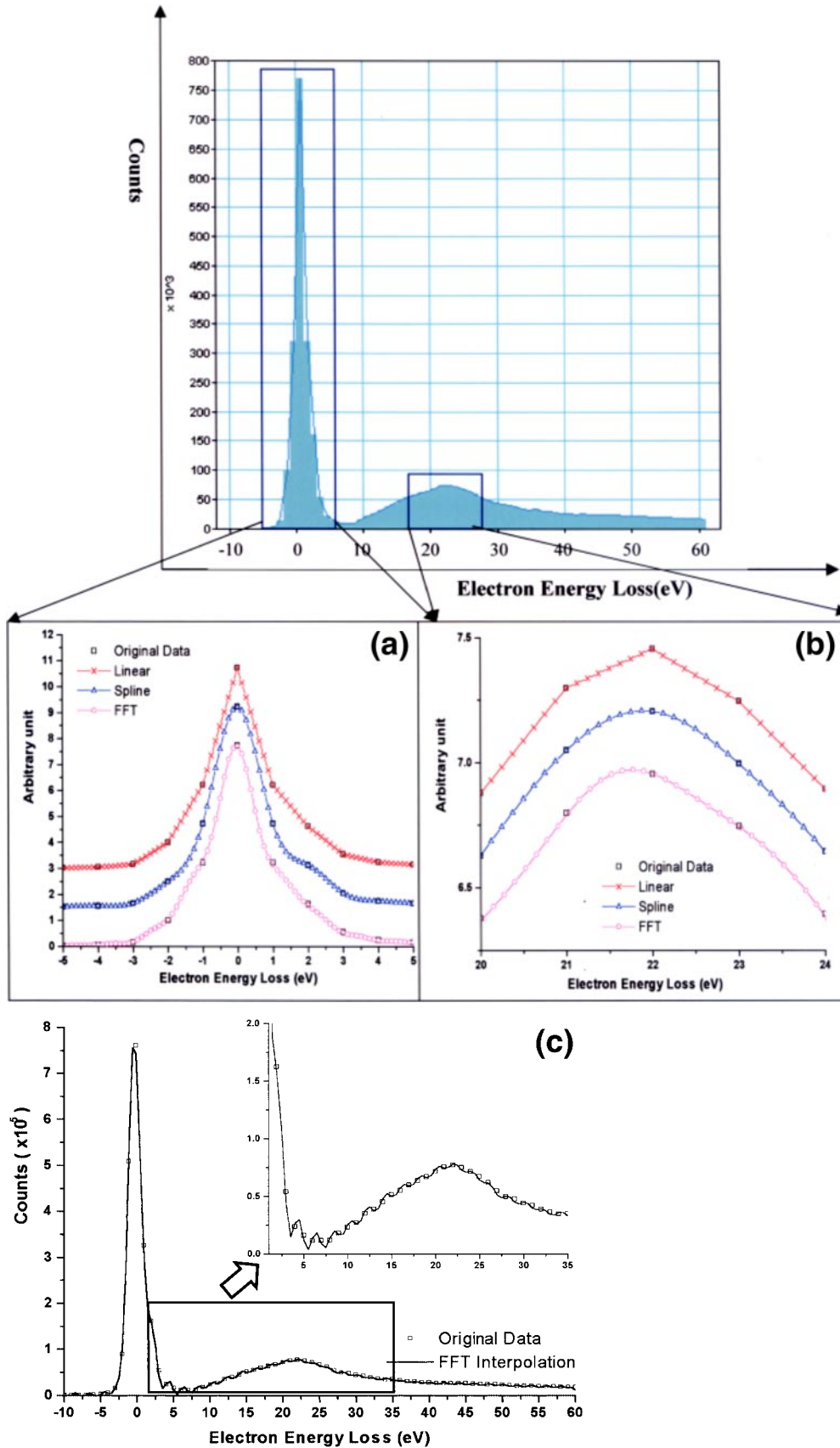


**Fig. 3** FFT, spline and linear interpolation in (a) the energy region of zero loss, and (b) the energy region of plasmon loss of Fig. 1b. (c) The artefacts of FFT interpolation arise from the spectrum contain huge intensity difference.

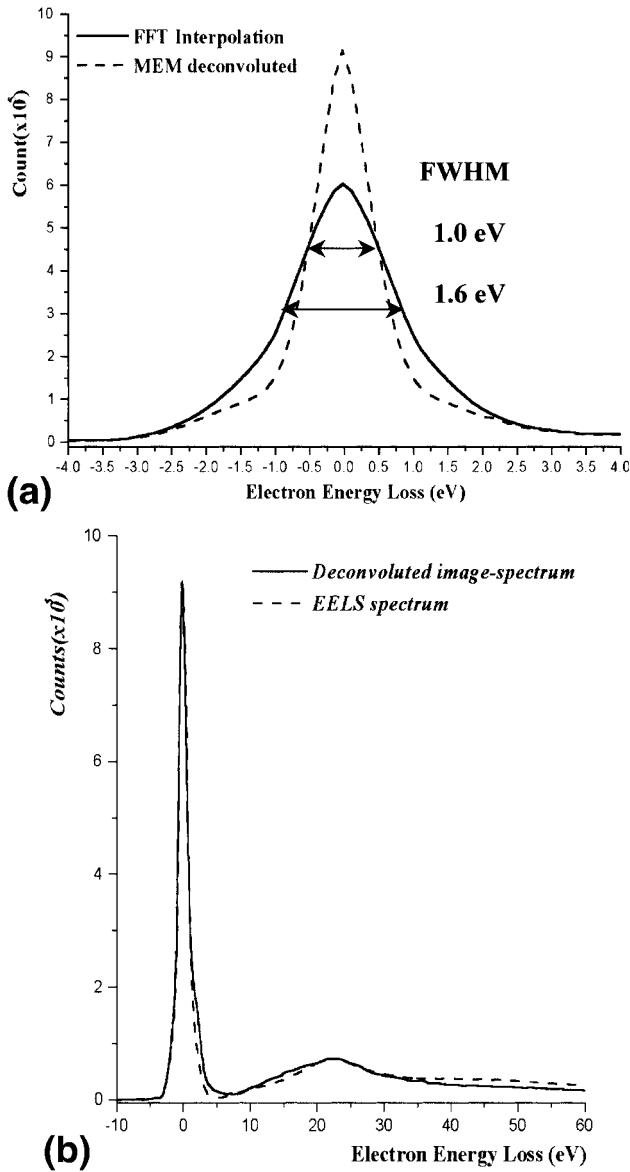


**Fig. 4** (a) Solid line is a FFT interpolated zero-loss peak and the dashed line is deconvoluted zero loss. The FWHM of a FFT interpolated spectrum is 1.6 eV and the energy resolution is improved to 1 eV after deconvolution. (b) A deconvoluted spectrum and an EELS spectrum acquired in image mode from the same position in BD.

term in Lagrangian function is the cross entropy, while the next two terms are the constraints for the optimum spectrum. The  $D(E_i)$  in the entropy term is a default guess that can be obtained by using a Wiener filter [31]. The  $\lambda_0$  and  $\lambda_1$  are two Lagrangian multipliers for two constraints. The first constraint sets the constant flux in the optimum solution  $S(E_i)$  and the second constraint sets the condition that the optimum  $S(E_i)$  convolutes with  $\text{PSF}(E_i)$  should be as close to be the  $S^{\text{exp}}$  as possible. This maximum entropy deconvolution method has been extensively used in the area of astronomy and signal processing to enhance the resolution of images (or signals) [32,33]. An example of maximum entropy deconvolution is

given in Fig. 4a. The solid line is a FFT interpolated spectrum of zero-loss peak in Fig. 1b reconstructed from the BD and the dashed line is the deconvoluted version of zero-loss peak. The FWHM of the FFT interpolated spectrum and the deconvoluted one are 1.6 and 1 eV, respectively. Apparently, the maximum entropy deconvolution improves the energy resolution of the EELS spectrum. The deconvoluted spectrum and an EELS spectrum acquired in image mode from BD are both shown in Fig. 4b. As we can see, reasonable agreement between these two spectra is obtained. The results indicate that the reconstructed spectrum from the ESI series images can be quantified with the almost same accuracy as the conventional EELS spectrum after FFT interpolation and maximum entropy deconvolution.

### Dielectric function analyses from Kramers–Kronig transformation and specimen thickness determination

The low-loss region of an EELS spectrum can provide the information of the energy-dependent dielectric function,  $\varepsilon(E) = \varepsilon_1 + i\varepsilon_2$  and also the direct band gap of materials [34–36] with Kramers–Kronig analysis [1,2]. Figure 5a is the zero-loss image of the images series in Fig. 1a. A three-dimensional visualization of the EELS spectra, as shown in Fig. 5b, was established from 46 image-spectra which were reconstructed along a line from A to B. The Si substrate and the other three dielectric layers have different characteristic plasmon peaks with Si 16.3 eV, SiO<sub>2</sub> 22.4 eV, Si<sub>3</sub>N<sub>4</sub> 20.7 eV and BD 22.1 eV, respectively. The double plasma peak exists in the Si region may be attributed to a plural scattering effect. Such plural scattering effect can easily be removed by using the Fourier-log deconvolution [37].

The relationship between single-scattering spectrum  $S(E)$  and the energy-loss function  $\text{Im}[-1/\varepsilon(E)]$  is given as

$$S(E) = \frac{I_0 t}{\pi a_0 m_0 v^2} \cdot \text{Im} \left[ \frac{-1}{\varepsilon(E)} \right] \cdot \ln \left[ 1 + \left( \frac{\beta}{\theta_E} \right)^2 \right] \quad (4)$$

where  $I_0$  is the zero-loss intensity,  $t$  the specimen thickness,  $a_0$  the first Bohr radius,  $m_0$  the electron mass,  $\beta$  the collection semi-angle, and  $\theta_E = E / (\gamma m_0 v^2)$  the characteristic scattering angle for an energy loss  $E$ . The real part of the dielectric function is related to the imaginary part by the Kramers–Kronig transformation [38]

$$\text{Re} \left[ \frac{1}{\varepsilon(E)} \right] = 1 - \frac{2}{\pi} P \int_0^\infty \text{Im} \left[ \frac{-1}{\varepsilon(E')} \right] \frac{E' dE'}{E' - E^2} \quad (5)$$

where  $P$  is the Cauchy principle part of the integral avoiding the pole at  $E = E'$ . Providing that the thickness of BD is known, the real and imaginary parts of the dielectric function of BD can be deduced from the  $S(E)$  by using eqs (4) and (5).

The specimen thickness  $t$  can easily be determined from the low-loss region of the EELS spectrum by using the log-ratio formula [39]

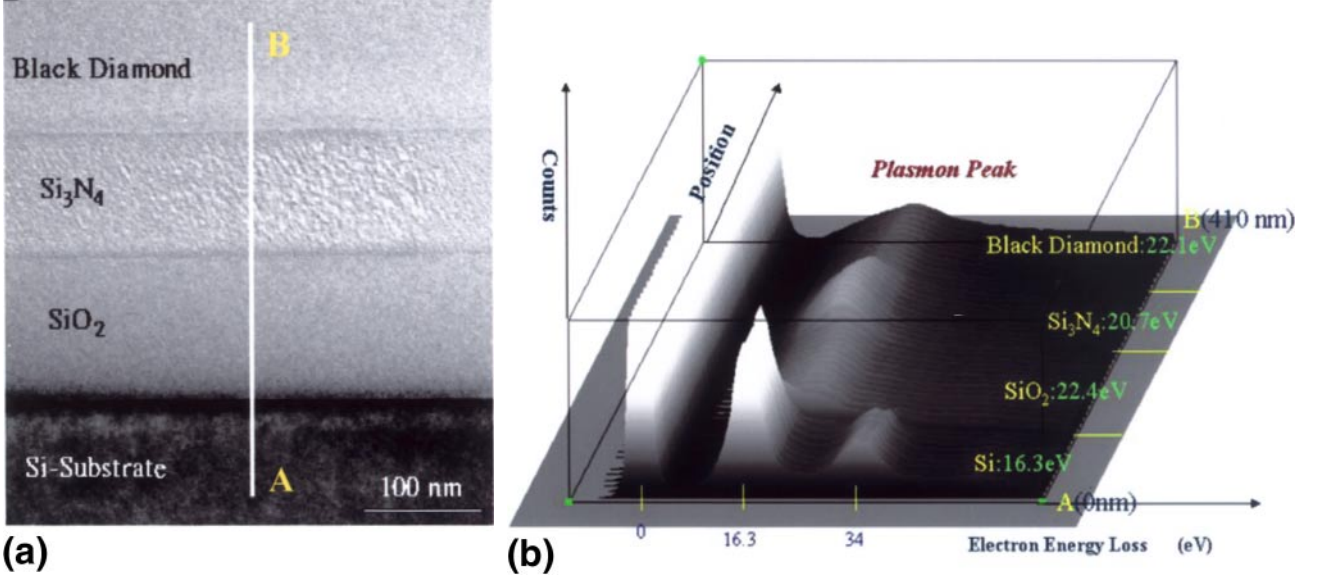


**Fig. 5** (a) The zero-loss image in the electron spectroscopic image series of BD / Si<sub>3</sub>N<sub>4</sub> / SiO<sub>2</sub> / Si in Fig. 1a. (b) A visualizing three-dimensional spectra reconstructed along A to B marked in Fig. 5a.

$$\left(\frac{t}{\lambda}\right) = \ln\left(\frac{I_t}{I_0}\right) \quad (6)$$

where  $I_t$  and  $I_0$  are integrals of the entire spectrum and of the zero-loss peak, respectively.  $\lambda$  is the inelastic mean free path, which is given as

$$\lambda(\text{nm}) = \frac{106F(E_0/E_m)}{\ln(2\beta E_0/E_m)} \quad (7)$$

where

$$E_m \approx 7.6Z_{\text{eff}}^{0.36}, \quad Z_{\text{eff}} = \frac{\sum_i f_i Z_i^{1.3}}{\sum_i f_i Z_i^{0.3}} \quad (8)$$

$$F = \frac{1 + E_0/1022}{(1 + E_0/511)^2}$$

$E_m$  is an average electron energy-loss in eV,  $Z$  is the atomic number,  $Z_{\text{eff}}$  is the effective atomic number of the specimen,  $f_i$  is the atomic fraction of the element of atomic number  $i$ , and  $F$  is the relativistic factor.

Equations (7) and (8) are empirical equations that may not give good estimation in thickness for BD. Furthermore, the application of the log-ratio method to BD has difficulty, since the  $Z_{\text{eff}}$  and  $E_m$  for BD are unknown in our sample. Besides, Malis *et al.* [39] and Yang and Egerton [40] have discussed that the accuracy in specimen thickness determination using the log-ratio method is about 15% accuracy. This implies that the accuracy in determination of the dielectric function will be not better than 15%. In fact, we have found that the dielectric function analysis is very sensitive to the thickness and sometimes gives an error larger than in the thickness.

In our experiment, absolute thickness of BD is obtained from an extrapolated thickness of Si / SiO<sub>2</sub> / Si<sub>3</sub>N<sub>4</sub>. The thicknesses of these three regions are determined from the low-loss

spectrum using Kramers–Kronig sum rule [41], providing that we know the refractive index  $n$  of these materials and that they are double checked using empirical eqs (7) and (8). The relationship of the thickness and  $n$  is given as

$$t = \frac{4a_0FE_0}{I_0\left(1 - \text{Re}\left[\frac{1}{\epsilon(0)}\right]\right)} \int_0^\infty \frac{S(E)dE}{E \ln(1 + \beta^2/0_E^2)} \quad (9)$$

where,  $\text{Re}\left[\frac{1}{\epsilon(0)}\right] = \frac{1}{n^2}$  and  $n$  is the refractive index of material.

The dielectric constant  $\epsilon(0)$  of a dielectric material (insulator) is the square of the refractive index. The dielectric constants are for Si, 11.36, for SiO<sub>2</sub>, 3.8, and for Si<sub>3</sub>N<sub>4</sub>, 3.6 [42]. The thickness of Si, SiO<sub>2</sub> and Si<sub>3</sub>N<sub>4</sub> can be determined from the  $S(E)$  of reconstructed spectra, using eq. (9) with a known dielectric constant. Figure 6a is a  $t/\lambda$  map obtained from the electron spectroscopic series images in Fig. 1a using eq. (6), while the profile  $t/\lambda$  from the position A to C is given in Fig. 6b. A thickness profile along A to C (Si to Si<sub>3</sub>N<sub>4</sub>) obtained using eq. (9) is shown in Fig. 6c, which has the same trend as that of  $t/\lambda$  profile. Plitzko and Mayer [12–14] have also shown the same kind of humps in the interface, and a similar thickness variation across the interface in the thickness map. We suspect that the humps in the thickness profile of the interface, between dissimilar materials, may arise from the focus shift due to different energy losses. Furthermore, the deviation of the thickness profile from the straight line may be partially caused by the elastic scattering contrast, or the different milling rates in different layers.

The average thickness profile suggests that the sample has a wedge shape. The accuracy of thickness determination can be improved and estimated by averaging as many profiles as possible. The thickness profile is fitted to a linear equation,  $Y =$

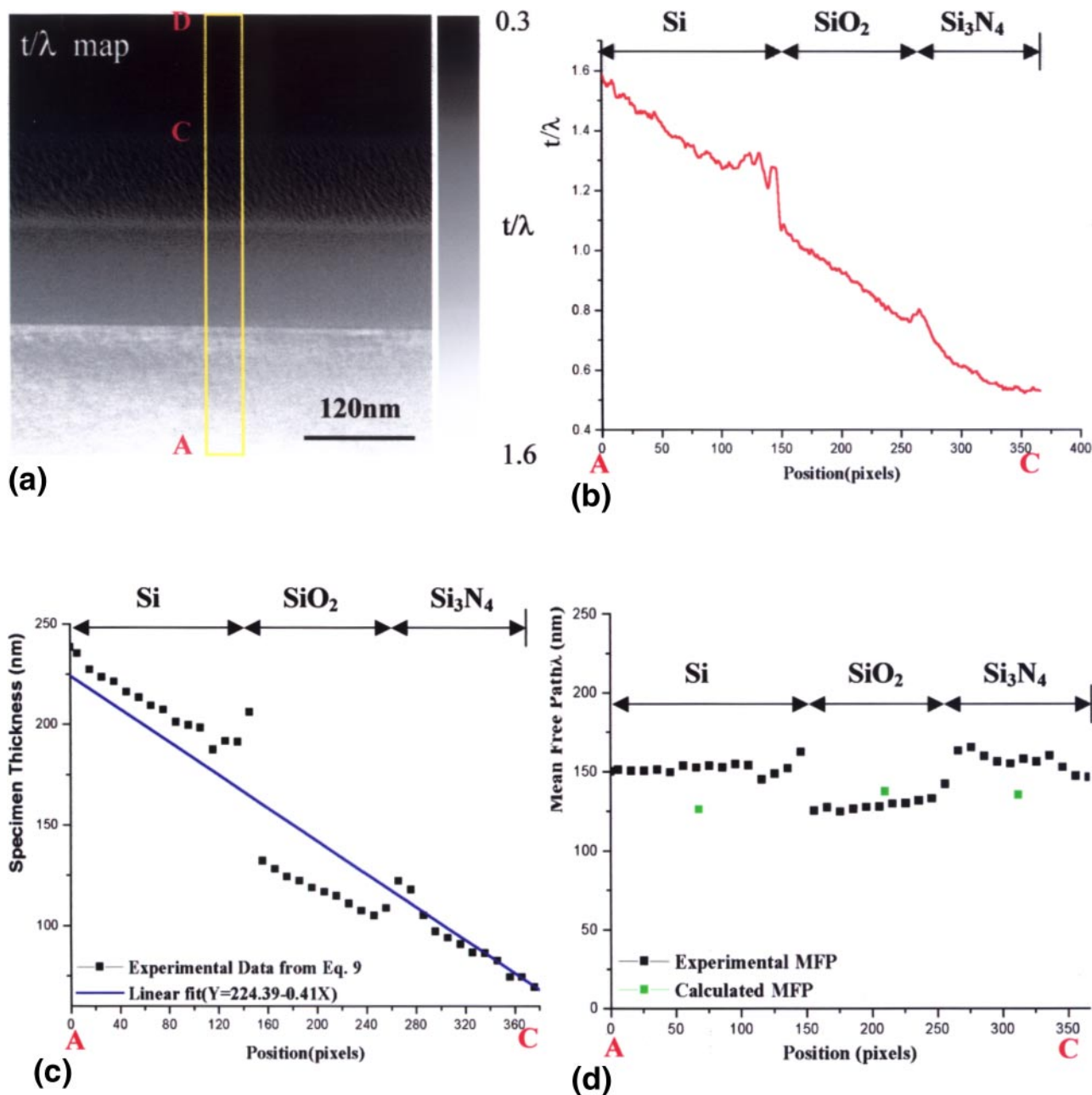


**Fig. 6** (a) The relative specimen thickness ( $t/\lambda$ ) map. The value of the  $t/\lambda$  is given as the grey scale bar on the right-hand side. (b) The profile of  $t/\lambda$  from position A to C. (c) A thickness profile determined from eq. (9) along the position A to C (Si to Si<sub>3</sub>N<sub>4</sub>) marked in Fig. 6a. (d) The line profile of mean free path that was determined from Figs 6b and 6c. The mean free path values calculated using eq. (7) are marked as squares.

224.39 – 0.41X (nm). The thickness in BD region can be determined by extrapolating the thickness profile to the BD region. The  $\lambda$  profile shown in Fig. 6d can be determined from Figs 6b and 6c. The value of  $\lambda$  approximates to a constant value in each material region and this might give an indication that the thickness profile in Fig. 6c is reasonably good. The  $\lambda$  values calculated using eq. (7) are marked as squares in Fig. 6d. The average values of  $\lambda$  of Si, SiO<sub>2</sub> and Si<sub>3</sub>N<sub>4</sub> determined from ESI series and the calculated data using eq. (7) are given in Table 1.

The extrapolated thickness of the BD from C to D varies roughly from 70 to 20 nm. The maps of the dielectric functions ( $\epsilon_1$  and  $\epsilon_2$ ) of BD/Si<sub>3</sub>N<sub>4</sub>/SiO<sub>2</sub>/Si can then be determined using eqs (4) and (5) by providing information from the thickness map. Such information is obtained from the  $t/\lambda$  map in Fig. 6a using  $\lambda_{exp}$  in the right hand column of Table 1. Figure 7 presents a dielectric constant map of the multilayer BD/Si<sub>3</sub>N<sub>4</sub>/SiO<sub>2</sub>/Si. The dielectric constant is a value that corresponds to the real part of dielectric function at zero energy loss. The image in the left-hand side of Fig. 7 is a part of zero-loss image

**Table 1** Values of mean free path. The calculated values are obtained using eq. (7). The experimental values are averaged from  $t/\lambda$  profiles, Fig. 6b, and the thickness profile, Fig. 6c.

Materials	$\lambda_{\text{cal}}$ (nm)	$\lambda_{\text{exp}}$ (nm)
Si	125.33	151.86 $\pm$ 3.68
SiO <sub>2</sub>	137.40	129.47 $\pm$ 4.91
Si <sub>3</sub> N <sub>4</sub>	135.15	152.87 $\pm$ 7.93
Black Diamond <sup>TM</sup>	None	127.01 $\pm$ 4.91

and the central image is the dielectric constant map of the same area. The average value of the dielectric constants of Si, SiO<sub>2</sub>, Si<sub>3</sub>N<sub>4</sub> and BD are calculated by summing the values in dielectric constant map and dividing the number of pixels in the corresponding materials region. The average dielectric constant of BD is 2.69  $\pm$  0.27, which is in good agreement with reference value (2.5  $\sim$  2.8) measured using the capacitance method [22]. The comparison between dielectric constant of four materials and reference data are given in Table 2. The average values of the dielectric constant for these four materials are 11.02  $\pm$  0.47, 4.20  $\pm$  0.31, 3.69  $\pm$  0.30, and 2.69  $\pm$  0.27, respectively, which are very close to their reference

**Table 2** Experimental dielectric constants and their reference data

Materials	$\epsilon_{\text{ref}}$	$\epsilon_{\text{exp}}$
Si	11.6	11.02 $\pm$ 0.47
SiO <sub>2</sub>	3.8	4.20 $\pm$ 0.31
Si <sub>3</sub> N <sub>4</sub>	3.6	3.72 $\pm$ 0.30
Black Diamond <sup>TM</sup>	2.5 $\sim$ 2.8	2.69 $\pm$ 0.27

**Table 3** The first peak of experimental dielectric functions ( $\epsilon_1$ ,  $\epsilon_2$ ) and their reference data

Materials	First peak of $\epsilon_1$	$\epsilon_{1\text{ref}}$	First peak of $\epsilon_2$	$\epsilon_{2\text{ref}}$
Si	4.0	3.25	3.5	3.75
SiO <sub>2</sub>	7.5	9	9	10
Si <sub>3</sub> N <sub>4</sub>	7.5	7	9	9.5
Black Diamond <sup>TM</sup>	8.5	None	9.5	None

Units: eV.

values 11.36, 3.8, 3.6 and 2.5  $\sim$  2.8 [42].

Turowski and Kelly used a field-emission STEM to record low-loss spectra as a function of position, across an Al / SiO<sub>2</sub> / Si field-effect transistor structure [43]. The authors showed the dielectric function across Al / SiO<sub>2</sub> / Si heterostructures; however, the line profile of dielectric function contained only one-dimensional spatial information. We propose that a four-dimensional property image presentation, which allows the uniformity of the energy dependent dielectric function, can be revealed in two dimensions. The four-dimensional dielectric property images of  $\epsilon_1$  and  $\epsilon_2$  are given in Fig. 8. The four dimensions refer to space ( $x$ ,  $y$ ), electron energy-loss (eV) and the dielectric function ( $\epsilon(E)$ ). Since there are abundant data in four dimensions, we present the property images only from a small portion of image and with 0.5 eV dispersion. The most left-hand side images in Figs 8a and 8b are a small portion of zero-loss image and the central parts are the real ( $\epsilon_1$ ) and imaginary part ( $\epsilon_2$ ) of dielectric property image, respectively. As shown in Figs 8a and 8b, each rectangular area, such as the one framed with a yellow dashed line, and equal in size to the zero-loss image, includes both spatial and dielectric function information,  $I(x, y, \epsilon_1 + i\epsilon_2)$  in one specific electron energy-loss value,  $\Delta E$ . Consequently, the dielectric property image includes four-dimensional  $I(\epsilon_1 + i\epsilon_2, x, y, \Delta E)$  information.

The  $\epsilon_1$  and  $\epsilon_2$  values of silicon vary abruptly, as shown in Fig. 8, while the dielectric function for BD shows the smoothest variation. The first peak of the dielectric function of each material was compared with reference data [42]. As shown in Table 3, the first peaks of the dielectric function ( $\epsilon_1$ ,  $\epsilon_2$ ) of all materials agree closely with reference data. The accuracy of the dielectric function depends on the accuracy of the thickness and the quality of the reconstructed spectra.

## Concluding remarks

We have developed FFT interpolation and maximum entropy deconvolution methods to overcome two problems, under-

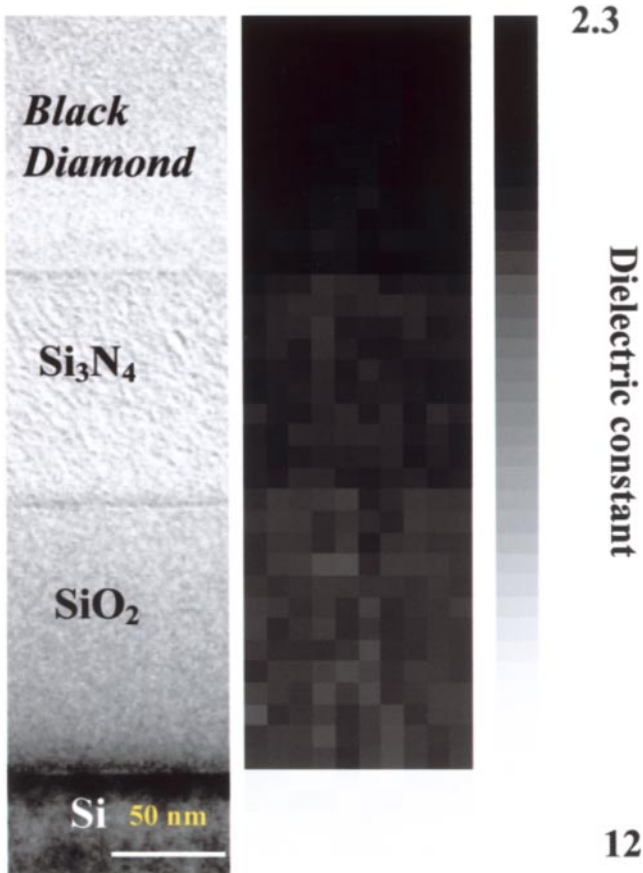


**Fig. 7** Dielectric constant map and the corresponding area in the zero-loss map. The value of the dielectric constant is given as the grey level bar on the right-hand side.

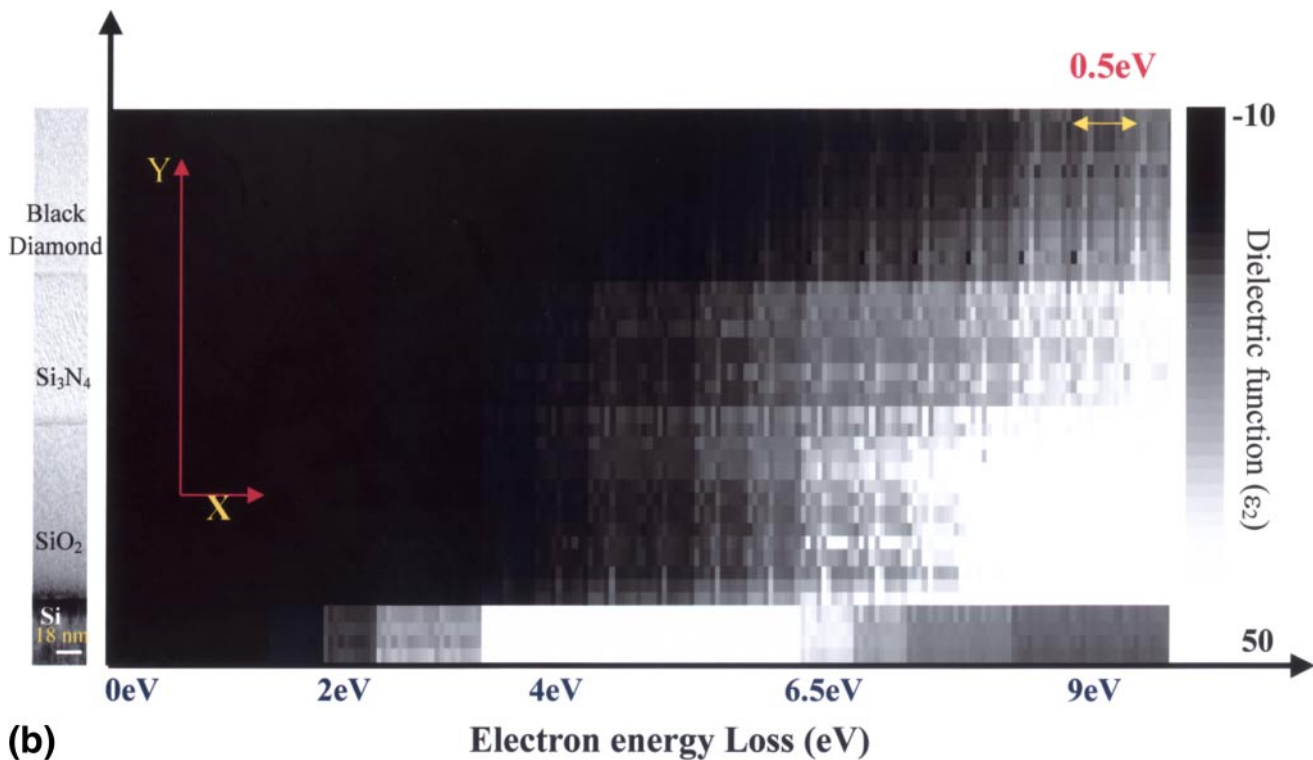
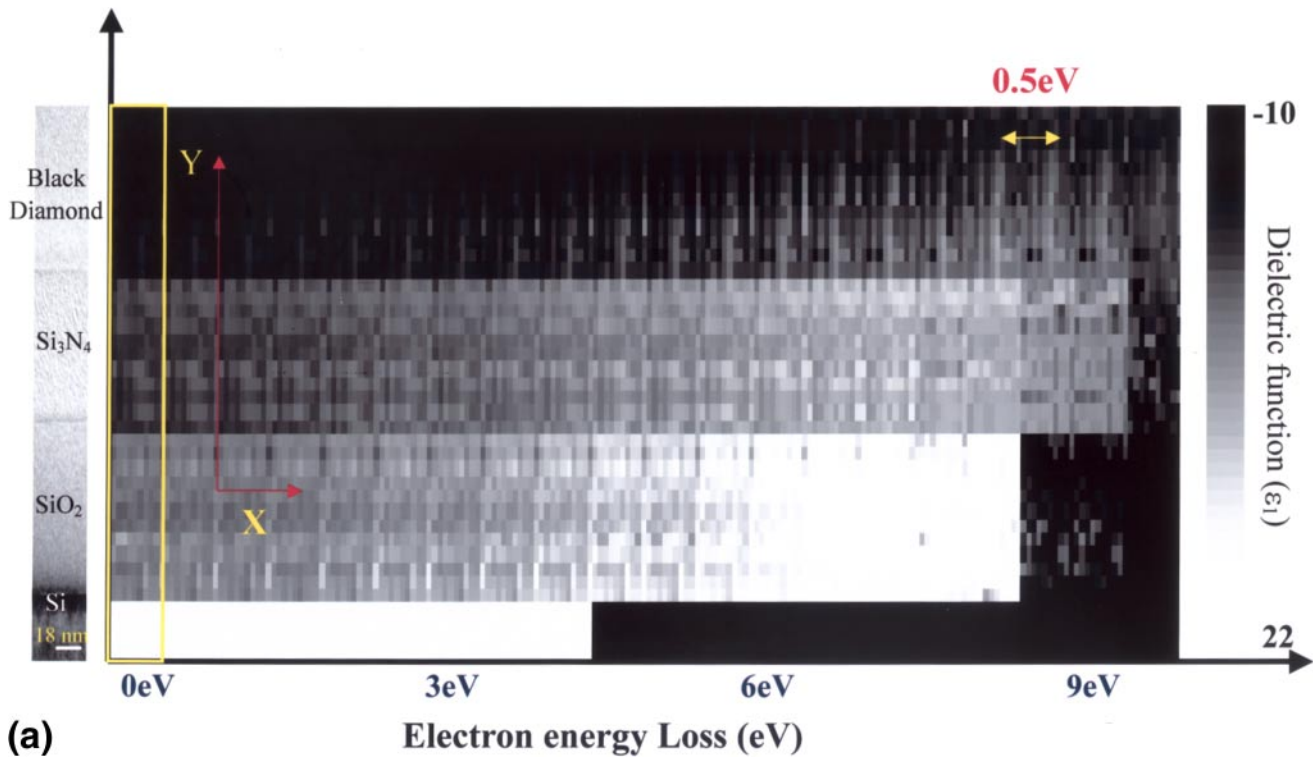


**Fig. 8** The dielectric property images. (a) The real part  $\epsilon_1$  and (b) imaginary part  $\epsilon_2$  of dielectric function. The most left-hand side images in (a) and (b) are a small portion of zero-loss image. The energy dispersion is 0.5 eV for both (a) and (b).

sampling and loss of energy resolution, in electron spectroscopic imaging series for quantitative analysis of dielectric function. Reconstructed spectra have shown the same resolution as that acquired with a focus beam. Since the analysis of

the dielectric function is sensitive to the local thickness of the specimen, we have determined the thickness of the BD using extrapolated thickness method from the materials of known dielectric constants. The dielectric function map can be

deduced from two-dimensional reconstructed single scattering spectra and the thickness using Kramers–Kronig analysis. We proposed a four-dimensional data presentation for revealing the uniformity of the energy dependent property. The accuracy of our methods depends on the thickness determination and the quality of the reconstructed spectra from the image series.

## Acknowledgements

Partial support of this work by the National Science Council of the Republic of China under Contract No. NSC89-2218-E007-056 is gratefully acknowledged.

## References

- Reimer L (1995) *Energy-Filtering Transmission Electron Microscopy*. (Springer-Verlag, New York.)
- Egerton R F (1996) *Electron Energy-Loss Spectroscopy in the Electron Microscope*. (Plenum Press, New York.)
- Hofer F, Grogger W, Warbichler P, and Papst I (2000) Quantitative energy-filtering transmission electron microscopy (EFTEM). *Mikrochim. Acta* **132**: 273–288.
- Grogger W, Hofer F, Warbichler P, and Kothleitner G (2000) Quantitative energy-filtering transmission electron microscopy in materials science. *Microsc. Microanal. Microstruct.* **6**: 161–172.
- Jeanguillaume C, Trebbia P, and Colliex C (1978) About the use of electron energy-loss spectroscopy for chemical mapping of thin foils with high spatial resolution. *Ultramicroscopy* **3**: 237–242.
- Krivanek O L, Gubbens A J, Kundmann M K, and Carpenter G C (1993) Elemental mapping with an energy-selecting imaging filter. In: *51st Ann. Proc. Electron Microsc. Soc. Am.*, pp. 586–587, (San Francisco Press, San Francisco).
- Jeanguillaume C and Colliex C (1989) Spectrum-image: the next step in EELS digital acquisition and processing. *Ultramicroscopy* **28**: 252–257.
- Lavergne J, Martin J, and Belin B (1992) Interactive electron energy-loss mapping by the ‘image-spectrum’ method. *Microsc. Microanal. Microstruct.* **3**: 517–528.
- Hunt J A and Williams D B (1991) Electron energy-loss spectrum imaging. *Ultramicroscopy* **38**: 47–73.
- Botton G and L’Esperance G (1994) Development, quantitative performance and applications of a parallel electron energy-loss spectrum imaging system. *J. Microsc.* **173**: 9–25.
- Bonnet N (1998) Multivariate statistical methods for the analysis of microscope image series: application in materials science. *J. Microsc.* **190**: 2–18.
- Mayer J, Eigenthaler U, Plitzko J M, and Dettenwanger F (1997) Quantitative analysis of electron microscopic imaging series. *Micron* **5**: 361–370.
- Marien J, Plitzko J M, Spolenak R, Keller R M, and Mayer M (1998) Quantitative electron spectroscopic imaging studies of microelectronic metallization layers. *J. Microsc.* **194**: 71–78.
- Plitzko J M and Mayer J (1999) Quantitative thin film analysis by energy filtering transmission electron microscopy. *Ultramicroscopy* **78**: 207–219.
- Thomas P J and Midgley P A (1999) Image-spectroscopy: new development and applications. *Microsc. Microanal.* **5** [Suppl. 2, Proceedings]: 618–619.
- Thomas P J and Midgley P A (1999) Fourier deconvolution of image-spectra: the removal of plural scattering from energy-filtered series. *Inst. Phys. Conf. Ser.* **161**: (EMAG 99) 179–182.
- Thomas P J, Midgley P A, and Spellward P (1999) Compositional mapping in the EFTEM using image-spectroscopy. *Inst. Phys. Conf. Ser.* **161**: (EMAG 99) 239–242.
- Thomas P J and Midgley P A (2000) Extended image-series analysis in the energy-filtered TEM. *EUREM* **12**: 1309–1310.
- Overwijk M H F and Reefman D (2000) Maximum-entropy deconvolution applied to energy-loss spectroscopy. *Micron* **31**: 325–331.
- Singhal K and Wlach J (1972) Interpolation using the fast Fourier transform. *Proc. IEEE* **1558**.
- Chen F R, Kai J J, Chang L, Wang J Y, and Chen W J (1999) Improvement of resolution by maximum entropy linear image restoration for NiSi<sub>2</sub>/Si interface. *J. Electron Microsc.* **48**: 827–836.
- Homma T (1998) Low dielectric constant materials and methods for interlayer dielectric films in ultralarge-scale integrated circuit multi-level interconnections. *Mat. Sci. Eng.* **R23**: 243–285.
- Pires F, Noël P, Le Cornec C, Passemard G, Louis D, and Lajoinie E (1997) Integration evaluation of low permittivity silicon based spin on materials as IMD. *Microelectron Eng.* **37/38**: 277–284.
- Private communication, Applied Materials, Santa Clara, CA, USA.
- Zhang H (1998) What limits the application of TEM in semiconductor industry? *Thin Solid Films* **320**: 77–85.
- Krivanek O L, Kundmann M K, and Kimoto K (1995) Spatial resolution in EFTEM maps. *J. Microsc.* **180**: 277–287.
- Digital Micrograph software (1997), © Gatan Inc., 66780 Owens Drive, Pleasanton, CA.
- Fraser D (1989) Interpolation by the FFT revisited – an experimental investigation. *IEEE Trans. Acoust., Speech, Signal Processing* **37**: 665–675.
- Schafer R W and Rabiner L R (1973) A digital signal processing approach to interpolation. *Proc. IEEE* **61**: 691–702.
- Chen F R, Kai J J, Ichnose H, and Chang L (2000) Extension of HRTEM resolution by semi-blind deconvolution method and Gerchberg–Saxton algorithm. *J. Electron Microsc.* (submitted).
- Gonzalez R C and Woods R E (1993) *Digital Image Processing*, pp. 253–304. (Addison-Wesley, Reading, MA.)
- Wilczek R and Drapatz A (1985) A high accuracy algorithm for maximum entropy image restoration in the case of small data sets. *Astron. Astrophys.* **142**: 9–12.
- Cornwell T J and Evans K F (1985) A simple maximum entropy deconvolution algorithm. *Astron. Astrophys.* **143**: 77–85.
- Bangert U, Harvey A J, and Keyse R (1997) Assessment of electron energy-loss spectroscopy below 5 eV in semiconductor materials in a VG STEM. *Ultramicroscopy* **68**: 173–180.
- Rafferty B and Brown L M (1998) Direct and indirect transitions in the region of the band gap using electron energy-loss spectroscopy. *Phys. Rev. B* **58**: 10326–10337.
- Rafferty B, Pennycook S J, and Brown L M (2000) Zero loss peak deconvolution for bandgap EEL spectra. *J. Electron Microsc.* **49**: 517–524.
- Egerton R F (1996) *Electron Energy-Loss Spectroscopy in the Electron Microscope*, pp. 246–254. (Plenum Press, New York.)
- Egerton R F (1996) *Electron Energy-Loss Spectroscopy in the Electron Microscope*, pp. 414–416. (Plenum Press, New York.)
- Malis T, Cheng S C, and Egerton R F (1988) EELS log-ratio technique for specimen measurement in the TEM. *J. Electron Microsc. Tech.* **8**: 8471–8477.
- Yang Y Y and Egerton R F (1995) Tests of two alternative methods for measuring specimen thickness in a transmission electron microscope. *Micron* **26**: 1–5.
- Egerton R F (1996) *Electron Energy-Loss Spectroscopy in the Electron Microscope*, p. 308. (Plenum Press, New York.)
- Palik E D (1998) *Handbook of Optical Constants of Solids III*, pp. 187–197. (Academic Press, London).
- Turowski M A and Kelly T F (1992) Profiling of the dielectric function across Al/SiO<sub>2</sub>/Si heterostructure with electron energy loss spectroscopy. *Ultramicroscopy* **41**: 41–54.